EPJ Web of Conferences **163**, 00008 (2017) DOI: 10.1051/epjconf/201716300008
FUSION17

Fission in Inverse Kinematics

A path to new experimental observables

Manuel Caamaño[1,⋆], *Fanny* Farget[2], and *Diego* Ramos[1,⋆⋆]

[1] *Universidade de Santiago de Compostela, E-15706 Santiago de Compostela, Spain*
[2] *GANIL, CEA/DSM-CNRS/IN2P3, BP 55027, F-14076 Caen Cedex 5, France*

Abstract. Historically, experimental fission studies were based on reactions in direct kinematics with fixed target-like fissioning systems. Besides its advantages, this technique suffers from some drawbacks such as the difficulty of producing exotic fissioning systems and the seldom measurement of the fragment atomic number. Inverse kinematic provides an alternative to ease these issues and offers a new set of experimental observables that improves our level of information about the fission process, including an unprecedented access to the scission point. In this document, we review some of the observables obtained from the experimental campaign based on inverse kinematics, performed at VAMOS/GANIL.

1 Introduction

Nuclear fission is a complex phenomenon in which the nucleus is deformed and heated, collective energy is dissipated in the form of intrinsic degrees of freedom, while the pairing and shell structure guide the process until two excited fragments are produced and accelerated due to their Coulomb repulsion.

Since its discovery, almost 80 years ago [1, 2], our current knowledge of fission was built on the interpretation of observables almost exclusively gathered in direct kinematics experiments: a heavy-nuclide target is bombarded by lighter projectiles that produce a target-like fissioning system. The properties of the fission products are measured to form the ensemble of experimental observables. Among them, direct kinematics allows the study of the fission probability, the fragments total kinetic energy, TKE, and mass distributions, their angular distribution, or the neutron evaporation. Together with the characterization of the fissioning system in terms of isotopic identification, excitation energy, etc., they shape the current image of fission: a process that runs along a potential energy formed by macroscopic and microscopic features of the nucleus, which depends sensitively on the number of protons and/or neutrons involved, and opens isolated deformation paths leading to different configurations at the scission point, called modes or channels [3, 4].

In spite of a wide opportunity of the fission setup in the direct kinematics method, it suffers from the following drawbacks: the small velocities of the emitted fragments disturb a good measurement of their the atomic number Z and impose restrictions to the amount of material in the target, while the use of direct kinematics limits systematic measurements to fissioning systems close in proton and neutron numbers to those of the target species. These difficulties can be overcome with the use of inverse kinematics: exotic nuclei can be produced with in-flight techniques and later guided to a secondary reaction target where fission can be induced; the measurement of the fragments Z distribution is also facilitated by their higher velocity when emitted from the moving fissioning systems.

The pioneering fission experiments with inverse kinematics at GSI [5] offered the measurement of Z and TKE distributions for a large number of neutron-deficient actinides [6], along the systematic measurement of the even-odd staggering [7], which is another scarce observable. Together, these observables revealed a fresh look on the role of protons and dissipation in the fission process. This is particularly interesting considering that shells are revealed in the number of protons and neutrons, and their effect is less evident in the mass distributions.

The last upgrade in the use of inverse kinematics was to include also the mass of the fragments, A, in the set of observables. The use of magnetic spectrometers allowed such improvement within two of the current experimental campaigns: SOFIA at GSI, which measures electromagnetic-induced fission of neutron-deficient systems [8, 9] with the help of the large dipole magnet ALADIN; and the fission campaign at GANIL, where fissioning systems around ^{238}U are studied through transfer- and fusion-induced fission using the VAMOS spectrometer [10, 11]. In the following, we discuss the collection of observables measured in the VAMOS/GANIL experiments.

⋆e-mail: manuel.fresco@usc.es
⋆⋆Present address: IPN Orsay, IN2P3/CNRS-UPS, F-91406 Orsay Cedex, France

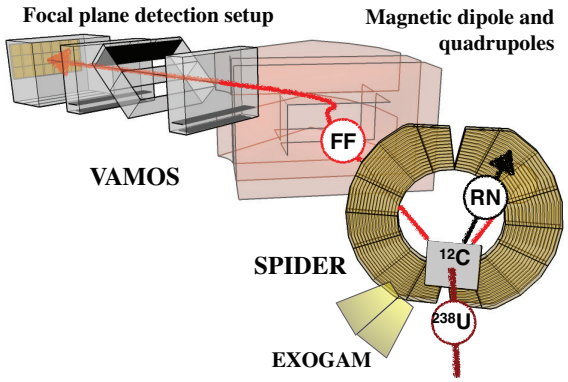

Figure 1. Schematic layout of the VAMOS setup during the first run of the fission campaign. After the transfer reaction, the target-like recoil (RN, black arrow) is measured in SPIDER, while one of the fission fragments (FF, red arrow) emitted after fission of the beam-like system is detected in the detector setup placed at the focal plane of the VAMOS spectrometer.

2 Transfer- and Fusion-Induced Fission in Inverse Kinematics at GANIL

As mentioned in the previous section, the fission campaign carried out at GANIL focused on the study of fission induced by direct reactions measured in the VAMOS variable mode spectrometer. A ^{238}U beam was shoot towards a ^{12}C target with 6.1 AMeV, an energy slightly above the Coulomb barrier, assuring the cross sections for transfer and fusion channels to reach tenths and hundreds of mb, respectively. Transfer reactions produced beam-like fissioning systems from U to Cm within a range of excitation energy, E^*_{FS}, below some 30 MeV, while fusion reactions resulted in ^{250}Cf with a fixed excitation energy of around 45 MeV.

The experimental setup can be laid out in two stages: the first one includes SPIDER, a set of two annular, double-sided, stripped silicon detectors devoted to the reconstruction of the direct reaction through the identification of the target-like recoil and the measurement of its angle and energy. A small part of the EXOGAM gamma detector is also placed to measure prompt gamma emission from the fragments. The second stage is based on the VAMOS spectrometer and its focal detectors, which detect one of the fission fragments for the isotope identification as well as the flight angle and velocity measurements. Figure 1 shows the VAMOS setup during the first run of the campaign. Further details can be found in Refs. [10–12]

The VAMOS setup offers a collection of observables carrying information from both the fissioning system and the produced fragments. For each fission event, the fissioning system is identified, and its E^*_{FS}, angle, and velocity are measured with the reconstruction of the direct reaction. Concerning the fission fragments, the use of inverse kinematics allowed, for the first time, the isotopic identification of the full fission fragment distribution [10]. Taking advantage of the features of transfer reactions, the evolution of the fission-fragment distributions on the Z-A plane can be studied as a function of the fissioning nuclides and their excitation energies [13]. In addition to Z and A, the fragments velocities and angles with respect to the beam direction are also measured, which, together with the identification and kinematics of the fissioning system, can be translated to the fissioning system reference frame. The simultaneous measurement of these characteristics allows to build new observables, offering new insights into the fission process. In the following sections we review and discuss some of these new observables.

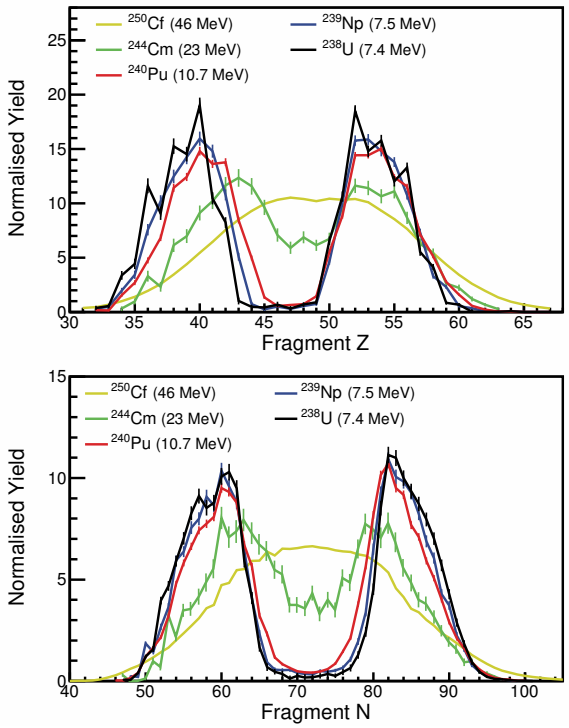

Figure 2. Fragment Z (top panel) and N (bottom panel) distributions for the fissioning systems measured in the second run of the VAMOS/GANIL campaign. The parentheses show the average excitation energy.

2.1 Neutron distribution and average neutron excess

The simultaneous measurement of the fragments Z and A distributions makes it possible to correlate both observables and build the neutron-number distribution for each event j, as N_j=A_j-Z_j. Such distribution corresponds to the fragments after post-scission neutron evaporation and thus it reflects the effect of neutron shells modified by the release of evaporated neutrons. Figure 2 shows the Z and post-evaporation N distributions for a set of systems with different average E^*_{FS}. The Z distributions of these systems show very similar features on the heavy fragment, with a clear preference for producing Z ~52, 54 fragments. However, the N distributions are more difficult to interpret. The pronounced peak around N=82 might be a combination of the influence of the neutron shell and the accumulation

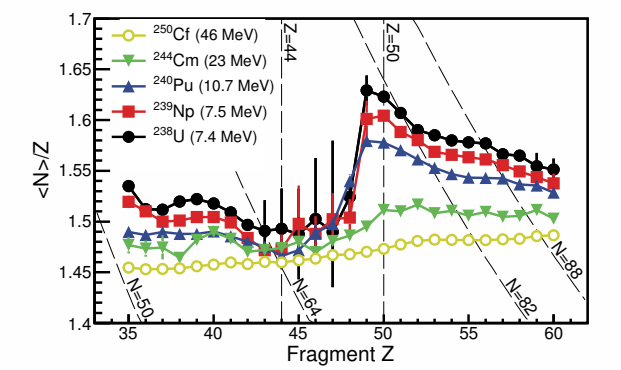

Figure 3. Fragment $\langle N\rangle/Z$ distribution for the fissioning systems measured in the second run of the VAMOS/GANIL campaign. The parentheses show the average excitation energy. The long-dashed lines correspond to proton and neutron numbers related to spherical and deformed shells.

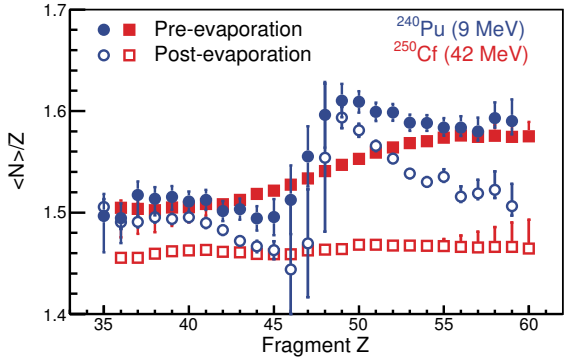

Figure 4. Pre-evaporation (open symbols) and post-evaporation (solid symbols) $\langle N\rangle/Z$ distributions for ^{240}Pu (blue dots) and ^{250}Cf (red squares) measured in the first run of the VAMOS/GANIL campaign. The parentheses show the average excitation energy.

of the end point of the neutron evaporation chains of its neighbors, which is coherent with the known minimum of evaporation for $A \sim 130$ (see [14, 15], for instance).

A degree of the magicity of nuclei affecting the fragments distribution can be represented by the neutron excess, defined as:

$$\langle N\rangle/Z = \frac{\sum(A-Z)\cdot Y(A,Z)}{\sum Y(A,Z)}, \qquad (1)$$

where $Y(A,Z)$ is the normalized yield of the A, Z fragment.

Figure 3 shows the $\langle N\rangle/Z$ distribution of the systems measured in the second run of the campaign. Despite the effect of neutron evaporation, a clear polarization is observed. Its shape evolve with $E^*_{\rm FS}$ until disappearing for ^{250}Cf, produced with $E^*_{\rm FS}$=46 MeV, suggesting that these features might be the result of the shell structure of the fragments. To explore this possibility we plot, in the same figure, the lines corresponding to proton and neutron numbers of relevant spherical and deformed shells [16].

We can see that the low-$E^*_{\rm FS}$ systems tend to approach the crossing of Z=50, N=82 spherical shells in the heavy fragments, and the crossing of Z=44, N=64 deformed shells in the light fragments. It is also worthy of note an accumulation around this point for all the systems, regardless of their $E^*_{\rm FS}$. The region around Z=44, N=64 is known to yield a high neutron multiplicity in the post-scission evaporation [14] but, at the same time, it was also observed to remain almost unaffected by the $E^*_{\rm FS}$ of the fissioning system [17].

2.2 Observables at the scission point

As mentioned in Sec. 2, the velocity of the fragments in the reference frame of the fissioning system can be determined with the reconstruction of the direct reaction producing the fissioning system and the measurement of the velocities of the fragments in the laboratory frame. Assuming that post-scission evaporation does not modify the velocity of the fragments, and applying the momentum conservation, the masses of the fragments at scission can be deduced [18]. In the case of the VAMOS/GANIL campaign, one fragment per fission event is measured and thus the observables calculated at scission are expressed as average quantities as a function of the fragment Z. Consequently, and unless stated otherwise, all quantities referred in this work to fragment properties are functions of the fragment Z. A full discussion of the method applied to these data can be found in [19].

Figure 4 shows the difference between the post-evaporation and pre-evaporation $\langle N\rangle/Z$ for ^{240}Pu with $E^*_{\rm FS}$=9 MeV and ^{250}Cf with $E^*_{\rm FS}$=42 MeV fission, both measured in the first run of the campaign. As we discussed in the previous section, the main features of pre-evaporation $\langle N\rangle/Z$ can be observed for low-$E^*_{\rm FS}$ systems. High-$E^*_{\rm FS}$ systems present a complete different picture before and after evaporation: the almost flat $\langle N\rangle/Z$ distribution of the post-evaporation ^{250}Cf data ($E^*_{\rm FS}$=42 MeV) is an outcome of the subtle counterbalance between the pre-evaporation $\langle N\rangle/Z$ value and the neutron emission, since both of them increase with Z. We can observe a clear change of slope around Z=54 that might be associated with the different evolution of deformed single-particle states in the regions between $44<Z<54$ and $55<Z$.

The access to Z, A, and velocity of the fragments at scission, combined with the identification of the fissioning system and its $E^*_{\rm FS}$, also permits to perform the energy balance between the input and output of the fission reaction. The input energy corresponds to the sum of the mass of the fissioning system, $M_{\rm FS}$, and its $E^*_{\rm FS}$. Considering no emission from saddle to scission, this is transformed into the ground-state masses of the fragments, M_1 and M_2, their total excitation energy, TXE, defined as the sum of the intrinsic and deformation energy of the fragments, and the total kinetic energy TKE, which is the sum of the Coulomb repulsion energy and the pre-scission kinetic energy. The energy balance is then

$$M_{\rm FS} + E^*_{\rm FS} = M_1 + M_2 + TKE + TXE. \qquad (2)$$

It is important to note that while $M_{\rm FS}$+$E^*_{\rm FS}$ is obtained from the reconstruction of the direct reaction, this quantity is, in

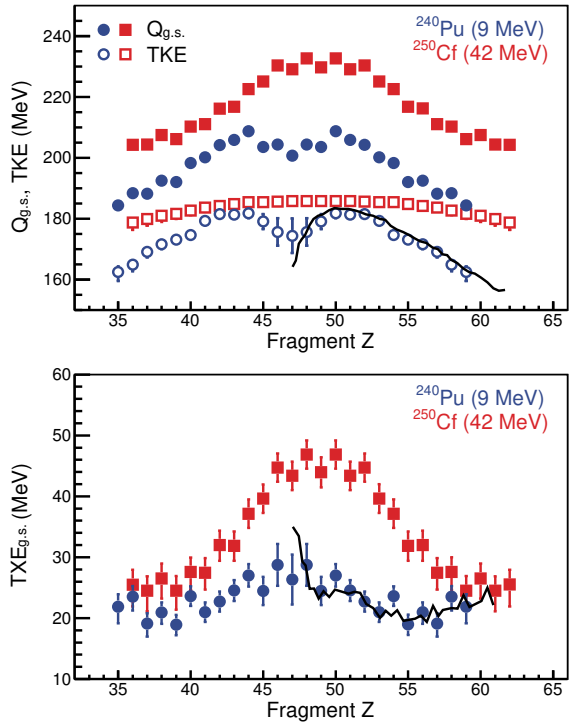

Figure 5. The figure shows the energy components for ^{240}Pu with E^*_{FS}=9 MeV (blue dots) and ^{250}Cf with E^*_{FS}=42 MeV (red squares). Top panel: TKE (open symbols) and $Q_{g.s.}$ (solid symbols); the black line is the TKE measured from ^{239}Pu(n$_{th}$,f) [15]. Bottom panel: $TXE_{g.s.}$; the black line is the $TXE_{g.s.}$ estimated from ^{239}Pu(n$_{th}$,f) [15].

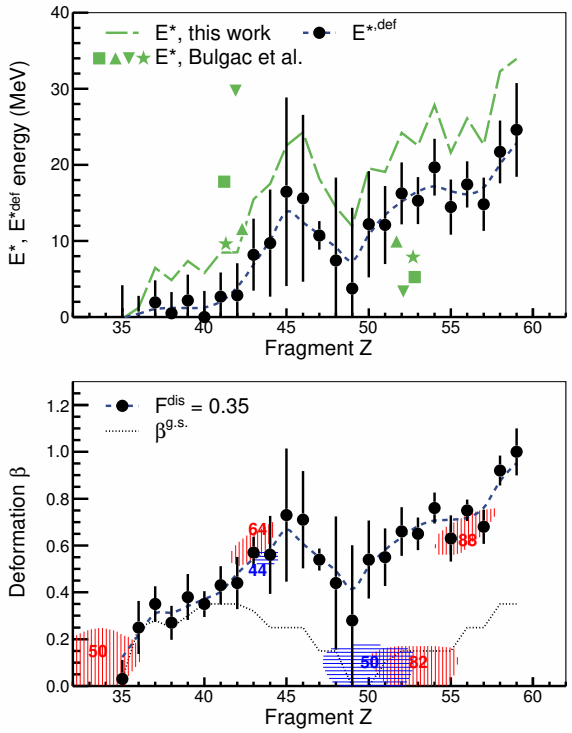

Figure 6. Top panel: E^* (green long-dashed line) and $E^{*,def}$ (black dots) of fragments produced in low-energy fission of ^{240}Pu. The blue dashed line is a moving average of the $E^{*,def}$ data. The green symbols correspond to results of the energy density functional model used in [28]. Bottom panel: Quadrupole deformation β (black dots) displayed with its moving average (blue dashed line). The hatched areas correspond to neutron (red) and proton (blue) spherical and deformed shells. The short-dashed black line is the average deformation at the ground state.

general, accurate for E^*_{FS} below the sum of the neutron separation energy and the fission barrier. For higher energies, an estimation of the pre-saddle evaporation is needed. As explained, M_1 and M_2 are obtained from the momentum conservation in the fissioning system reference frame, while TKE is calculated with the velocities in the same reference frame. From these quantities is possible to calculate the distribution of both the average $TXE_{g.s.}$ and the $Q_{g.s.}$ value at the ground state of the reaction, defined as

$$TXE_{g.s.} = M_{FS} - M_1 - M_2 - TKE = Q_{g.s.} - TKE. \quad (3)$$

Figure 5 shows the resulting TKE, $Q_{g.s.}$, and $TXE_{g.s.}$ at scission for ^{240}Pu with E^*_{FS}=9 MeV and ^{250}Cf with E^*_{FS}=42 MeV, both from the first run of the campaign. A first glance at the top panel shows a very similar behavior for both TKE and $Q_{g.s.}$ in the case of the low-energy fission of ^{240}Pu. This similarity was already hinted in previous studies of cold fission in light actinides, where the contribution of TXE is at minimum [20]. In the case of high-energy fission of ^{250}Cf, the similarity between TKE and $Q_{g.s.}$ disappears around the symmetry, where a difference builds up. Concerning $TXE_{g.s.}$, the bottom panel of Fig. 5 shows an almost flat distribution for low energy fission, with an increase of almost 10 MeV around the symmetry. However, the case of high-energy fission shows the $TXE_{g.s.}$ growing from ~ 25 MeV at asymmetric splits to ~ 45 MeV around the symmetry.

The results of TKE and $TXE_{g.s.}$ in ^{240}Pu are also compared in Fig. 5 with previous studies of ^{239}Pu(n$_{th}$,f) [15]. The overall values of TKE and $TXE_{g.s.}$ are in agreement with the present data with the exception of the symmetric split, where a larger TKE and a smaller $TXE_{g.s.}$ are obtained in the present data. This difference is likely to be a combination of the larger excitation energy of the fissioning system and the limited resolution of the present experiment for symmetric splits due to the lower statistics.

2.3 Energetics and configuration at scission

The fission observables discussed so far permit, combined with reasonable assumptions, to extract more information on the scission configuration of the fragments, such as their excitation energy, deformation, and distance. The details of such calculation can be found in [23]

The measured TXE is the sum of the excitation energy E^*_i of each fragment i.[1] These can be separated into each fragment deformation energy $E^{*,def}_i$ and intrinsic energy, which is the sum of the initial excitation energy above the

[1] As previously mentioned, with this setup we deal with average quantities per fragment Z. Since we detect one fragment per fission, the average properties of fragment Z are correlated with those of fragment Z_{FS}-Z

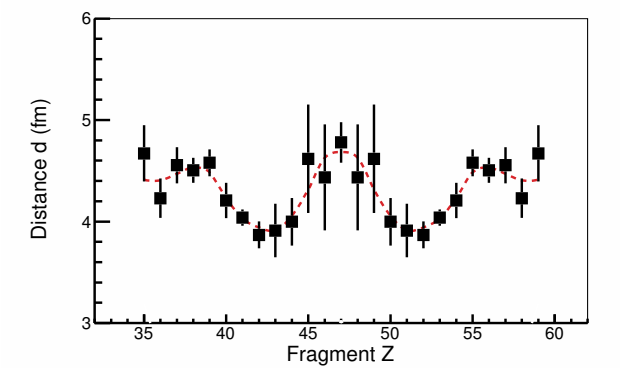

Figure 7. Tip distance between the fragments (symbols). The red dashed line is a moving average of the data.

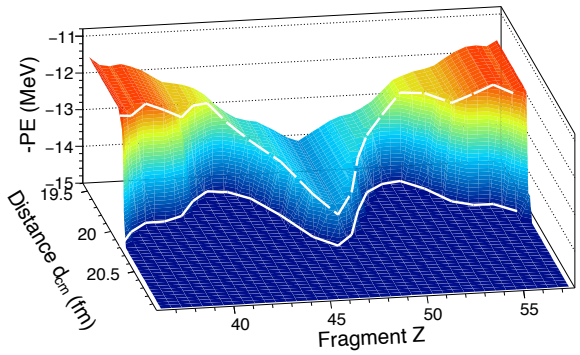

Figure 8. Potential landscape at scission. The white dashed line corresponds to a moving average of the scission point as a function of PE, $d_{\rm cm}$, and Z. The white solid line shows the projection onto the $d_{\rm cm}$-Z plane.

barrier $E_i^{*,\rm Bf}$ and the dissipated energy along the process $E_i^{*,\rm diss}$:

$$TXE = \sum_{i=1}^{2} E_i^* = \sum_{i=1}^{2} \left(E_i^{*,\rm Bf} + E_i^{*,\rm dis} + E_i^{*,\rm def} \right). \quad (4)$$

Experimentally, TXE is fully released in the form of neutron and γ evaporation:

$$TXE = \sum_{i=1}^{2} \left(Q_i^n + \nu_i \varepsilon_i + E_i^\gamma \right), \quad (5)$$

where ν_i is the neutron multiplicity, ε_i is the neutron kinetic energy, E_i^γ is the energy released by γ emission, and Q_i^n is the difference between pre- and post-evaporation fragment masses. Previous data show that the average ε is approximately symmetric with respect to the fragments split [14], and that E_i^γ follows the behavior of ν_i with a total value similar to the neutron separation energy S_n [24]. These properties allow to express Eq. 5 as

$$TXE \approx \sum_{i=1}^{2} Q_i^n + \nu_i \left(\varepsilon + S_n/(\nu_1 + \nu_2) \right). \quad (6)$$

ν_i and Q_i^n are measured observables, while S_n is calculated as the average neutron separation energy for each split.

The combination of Eqs. 4 and 6 permits to deduce $E_i^{*,\rm def}$, once the part $E_i^{*,\rm Bf}$+$E_i^{*,\rm dis}$ is shared between the fragments in a regime of statistical equilibrium, following the prescription of Refs. [25, 26]. Concerning the dissipation energy, in this work we followed the prescription of Ref. [27], where the dissipation is a fixed fraction of the available TXE.[2] These approximations and prescriptions are valid for low-energy fission of actinides and, in our case, we applied them to the ^{240}Pu data at $E_{\rm FS}^*$=9 MeV. The top panel in Fig. 6 shows the distribution of the excitation energy E_i^* and the fraction dedicated to deformation, $E_i^{*,\rm def}$. The E_i^* data is compared with a recent calculation based on a real-time, microscopic framework of energy density functional [28], also applied to low-energy fission of ^{240}Pu. We can see what the authors interpret as a quasi-spherical slightly-excited heavy fragment around Z=52 and a highly-deformed highly-excited light one around Z=42. There is a fair discrepancy with our results: at Z ~52 we find deformed fragments excited up to 20 MeV, while at Z ~42 we have similarly deformed fragments with an excitation energy of ~10 MeV.

It is also worthy to mention the relatively high multiplicity around Z=50: the literature shows multiplicities of the order of ν ~0.5 around the corresponding masses (see [15, 17] for example). In the present case, the excess of ν can be explained, at least in its most part, with the $E_{\rm FS}^*$ induced by the transfer reaction. Other factors, such as an increase of the deformation or a lower fission barrier due to the angular momentum, might also play a role.

The bottom panel of Fig. 6 shows the translation of $E^{*,\rm def}$ into quadrupole deformation β by computing the increase in energy of the Weizsäcker liquid-drop mass-formula for variations in the surface and Coulomb terms due to small quadrupole deformations, following the prescription of Swiatecki [29]. We can see that β retains the well-known sawtooth shape already observed in ν and E^*, while it runs through Z=44, N=64, 88 deformed shells. It is also interesting that, although β is "pulled" towards lower values around Z=50, N=82 spherical shells, the deformation is relatively high. The competition between single particle structure and the macroscopic potential, which is particularly strong close to symmetry, seems to hinder the effect of these spherical shells.

Once the deformation of the fragments are known, the tip distance between the fragments, d, can be extracted with the measured TKE, which is the sum of the contribution from the Coulomb repulsion between the fragments, $E^{\rm k,C}$, and the pre-scission kinetic energy, $E^{\rm k,pre}$:

$$TKE = E^{\rm k,C}(Z_1, Z_2, \beta_1, \beta_2, d) + E^{\rm k,pre}(Z_1, Z_2), \quad (7)$$

In this case, we use $E^{\rm k,pre}$ from a two-center shell-model parameterization, calculated as a function of the fragment [30]. The tip distance d is then deduced from $E^{\rm k,C}$ following the Cohen-Swiatecki formula [31]. The resulting distance d is displayed in Fig. 7. We observe values between 4 and 5 fm, further than the "standard" 2-3 fm of low-energy fission of actinides [3, 16, 32–35] but similar

[2] A complete discussion of the convenience of these prescriptions can be found in [23].

to the values used in recent scission-point models [36]. We can also see that configurations around Z_1=42, Z_2=50 are more compact than those at symmetric and very asymmetric splits. This minimum coincides with a maximum in TKE, suggesting a correlated behavior between both the TKE and d, and also with shell effects.

The TXE discussed so far corresponds to the total excitation energy gained by the fragments at scission with respect to their ground states. We can recover the potential energy surface by expressing the total excitation energy with respect to the deformed ground states of the fragments (see for example [21, 22]). Together with the calculated $E^{*,\mathrm{def}}$, β_i, and d, they can be combined to outline the shape of the potential energy PE landscape that the system experiences at scission, defined as

$$PE = TXE - E_1^{*,\mathrm{def}} - E_2^{*,\mathrm{def}}, \tag{8}$$

with the distance between the centers of the fragments d_{cm}:

$$d_{\mathrm{cm}} = d + r_0 A_1^{1/3}\left(1 + \sqrt{\frac{5}{4\pi}}\beta_1\right) + r_0 A_2^{1/3}\left(1 + \sqrt{\frac{5}{4\pi}}\beta_2\right), \tag{9}$$

to obtain the PE-d_{cm}-Z correlation at scission. The result is displayed in Fig. 8. The potential energies at scission appear with a prominent minimum of some 10 MeV smaller than the asymmetric splits, which coincides with an elongated shape. At the same time, the distance between fragments is still smallest around Z_1=42, Z_2=50, meaning the system breaks sooner when affected by microscopic effects. The fact that the macroscopic potential at symmetry is observed in the depth of the landscape with no apparent structure effects suggests a strong connection between these effects and the elongation that the system can reach before splitting.

3 Conclusions

The use of inverse kinematics in new experimental campaigns allows to obtain simultaneously a number of observables that were historically difficult to access and always in separate experiments, such as the fragment A, Z, and velocity distributions. The correlation of these observables permitss to construct new quantities with improved sensitivity to fission properties. The neutron excess, and the TXE and TKE at scission are now available for different systems and as a function of the fission energy. In some cases, such as low-energy fission of actinides, the new observables can be extended to reveal the energy sharing and the configuration at scission, in terms of deformation and distance of the fragments. These results help to better understand the role of structure effects in the process and contribute to the pool of experimental fission data to be compared with state-of-the-art models.

Acknowledgements

M.C. acknowledges the financial support of the Program "Ramón y Cajal" of the Ministerio de Economía y Competitividad of Spain through the grant RYC 2012-11585.

References

[1] O. Hahn and F. Strassmann, Naturwiss **27**, 11 (1939)
[2] L. Meitner and O. Frisch, Nature **143**, 239 (1939)
[3] U. Brosa *et al.*, Phys. Reports **197**, 167 (1990)
[4] M.G. Itkis *et al.*, Z. Phys. A - Atoms and Nuclei **320**, 433 (1985)
[5] K.-H. Schmidt *et al.*, Nucl. Phys. A **665**, 221 (2000)
[6] C. Böckstiegel *et al.*, Nucl. Phys. A **802**, 12 (2008)
[7] S. Steinhäuser *et al.*, Nucl. Phys. A **634**, 89 (1998)
[8] J.-F. Martin *et al.*, Eur. Phys. J. A **51**, 174 (2015)
[9] E. Pellereau *et al.*, Phys. Rev. C **95**, 054603 (2017)
[10] M. Caamaño *et al.*, Phys. Rev. C **88**, 024605 (2013)
[11] C. Rodríguez-Tajes *et al.*, Phys. Rev. C **89**, 024614 (2014)
[12] D. Ramos, "Fragment Distributions of Transfer- and Fusion-Induced Fission from ^{238}U+^{12}C Reactions Measured Through Inverse Kinematics" PhD (Univ. of Santiago de Compostela, 2016)
[13] D. Ramos *et al.*, EPJ Web Conf. **111**, 10001 (2016)
[14] K. Nishio *et al.*, Nucl. Phys. A **632**, 540 (1998)
[15] C. Tsuchiya *et al.*, J. Nucl. Sci. Technol. **37**, 941 (2000)
[16] B.D. Wilkins *et al.*, Phys. Rev. C **14**, 1832 (1976)
[17] K.-H. Schmidt and B. Jurado, Phys. Rev. Lett. **104**, 212501 (2010)
[18] H.C. Britt *et al.*, Nucl. Instrum. Methods **24**, 13 (1963) and references therein
[19] M. Caamaño *et al.*, Phys. Rev. C **92**, 034606 (2015)
[20] F. Gönnenwein, Z. Phys. A **349**, 259 (1994)
[21] P. Möller *et al.*, Phys. Rev. C **79**, 064304 (2009)
[22] J. Randrup and P. Möller, Phys. Rev. Lett. **106**, 132503 (2011)
[23] M. Caamaño and F. Farget, Phys. Lett. B **770**, 72 (2017)
[24] R. Capote *et al.*, Nucl. Data Sheets **131**, 1 (2016), and references therein.
[25] R. Capote *et al.*, Nucl. Data Sheets **110**, 3107 (2009)
[26] K.-H. Schmidt and B. Jurado, Phys. Rev. C **83**, 061601(R) (2011)
[27] F. Rejmund *et al.*, Nucl. Phys. A **678**, 215 (2000)
[28] A. Bulgac *et al.*, Phys. Rev. Lett. **116**, 122504 (2016)
[29] W.J. Swiatecki, Phys. Rev. **104**, 993 (1956)
[30] F.A. Ivanyuk *et al.*, Phys. Rev. C **90**, 054607 (2014)
[31] S. Cohen and W.J. Swiatecki, Annals of Physics **19**, 67 (1962)
[32] T.-S. Fan *et al.*, Nucl. Phys. A **591**, 161 (1995)
[33] C. Böckstiegel *et al.*, Nucl. Phys. A **802**, 12 (2008)
[34] H. Goutte *et al.*, Phys. Rev. C **71**, 024316 (2005)
[35] K.-H. Schmidt *et al.*, Nucl. Data Sheets **131**, 107 (2016)
[36] J.-F. Lemaître *et al.*, Phys. Rev. C **92**, 034617 (2015)